Metals on oxides: structure, morphology and interface chemistry

2007 J. Phys.: Condens. Matter 19 225002

(http://iopscience.iop.org/0953-8984/19/22/225002)

IOP PUBLISHING JOURNAL OF PHYSICS: CONDENSED MATTER

J. Phys.: Condens. Matter **19** (2007) 225002 (24pp) doi:10.1088/0953-8984/19/22/225002

Metals on oxides: structure, morphology and interface chemistry

S Valeri[1,2,3], **S Benedetti**[1,2] **and P Luches**[1]

[1] S3, CNR-INFM, Via G Campi 213/a, I-41100 Modena, Italy
[2] Department of Physics, University of Modena and Reggio Emilia, Via G Campi 213/a, I-41100 Modena, Italy

E-mail: valeri@unimo.it

Received 28 June 2006, in final form 3 August 2006
Published 14 May 2007
Online at stacks.iop.org/JPhysCM/19/225002

Abstract

In this paper we review our recent studies on the structure, morphology and interface chemistry of different metal systems on simple rock-salt oxides, providing a basis for the understanding of their properties.

Fe on both MgO and NiO grows in the cubic structure with the (001)Fe ∥ (001)oxide and [110]Fe ∥ [100]oxide orientation.

The Fe/MgO interface is sharp at the atomic level up to 400 °C, thus showing that MgO can allow the growth of 'free standing' Fe films and low-dimensional structures. Submicrometric Fe dots on MgO have been prepared by FIB milling and characterized by the magneto-optical Kerr effect. At the Fe/NiO(001) interface an Fe–Ni body centred tetragonal alloyed phase is formed on top of a two-dimensional FeO layer situated at the interface. The FeO layer presents an expansion of the interplanar distance at the interface and a buckling in the Fe and O atomic positions. The presence of the structurally distorted FeO phase is predicted by *ab initio* density functional theory calculations to increase the spin magnetic moment of Fe atoms by 0.6 μ_B compared to the ideally abrupt interface. A reduction of NiO is also induced by the deposition of (supposedly) inert Au films, which incorporate the metallic Ni atoms. The reduction takes place at the low-coordination sites at the surface of the NiO film. The Co/MgO(001) system has also been studied. In all the investigated cases, given the lower surface free energy of the oxide surfaces compared to the metal ones, the deposited metals tend to form islands, which coalesce above a few monolayers.

(Some figures in this article are in colour only in the electronic version)

[3] Author to whom any correspondence should be addressed.

1. Introduction

The control and optimization of the properties of low-dimensional metallic systems on oxides require an atomic level characterization of their structure, morphology and chemistry. This aspect is very important for the technological applications, which are gradually moving towards active elements with dimensions in the nanometre scale, in which the influence of interfaces, surfaces and defects plays a crucial role.

The fields of application of these materials range from catalysis to magnetoelectronics and optics [1]. Oxide supported metal particles have been shown to have size dependent catalytic activity, even for materials which are inert in their bulk phase [2, 3]. In information storage technology, metal on oxide nanocomposite materials present promising applications [4]. The strong influence of the quality of their interfaces, in terms of roughness, interdiffusion, chemical state and geometric structure, on the properties of the materials has been widely recognized [5–7]. In magnetic tunnel junctions, for example, the tunnelling current between two ferromagnetic layers through the non-magnetic layer has been shown to be strongly affected by the presence of magnetic oxides or nonmagnetic metal layers at the interface [8]. Also exchange bias, i.e. the unidirectional anisotropy resulting from interfacial exchange interaction between FM and AFM materials, still lacks a satisfactory explanation [4, 9], partly due to the still incomplete picture of the morphology, chemistry and structure of the interfaces at the atomic scale.

In this paper we review the results obtained on some simple epitaxial systems in this field. The oxides on which we focus have the rock-salt structure and the chosen metals have a lattice mismatch with the oxide within a few per cent, allowing a good epitaxial growth in most of the investigated cases. Complementary ultra-high-vacuum (UHV) spectroscopic and microscopic techniques, combining integrated and local probes, have been used to obtain a complete characterization in terms of structure, morphology and chemistry.

2. Oxide substrates

2.1. NiO(001)

NiO is a very interesting antiferromagnetic material with a simple rock-salt structure and a Néel temperature significantly higher than room temperature. It is widely studied both in the field of electron correlation in solids [10, 11] and for its appealing application in magnetoelectronic devices [4, 9].

The NiO(001) surface can be prepared by cleavage in air of a NiO single crystal, followed by UHV annealing at 400 °C for 30 min. In this way a surface free of contaminants within the x-ray photoelectron spectroscopy (XPS) sensitivity can be obtained. The use of NiO in the form of films on metal substrates allows us to study the evolution of the properties with increasing thickness. These systems can be investigated by electron spectroscopies and scanning tunnelling microscopy without charging problems up to a few nanometres NiO thickness. NiO films with a very good crystal quality exposing the (001) surface can be UHV grown on Ag(001) by evaporating Ni in O_2 partial pressure (reactive growth) [12, 13]. For NiO thickness below 2 ML a strong dependence of structure and composition on the oxygen-to-nickel flux ratio has been observed. A low oxygen dosage induces a (2×1) reconstruction in the 1 ML films that evolves to a (1×1) phase as the dosage and/or the film thickness increases [14]. For higher NiO thickness we have shown by XPS and Auger electron spectroscopy (AES) that the films are stoichiometric [13]. Primary beam diffraction modulated

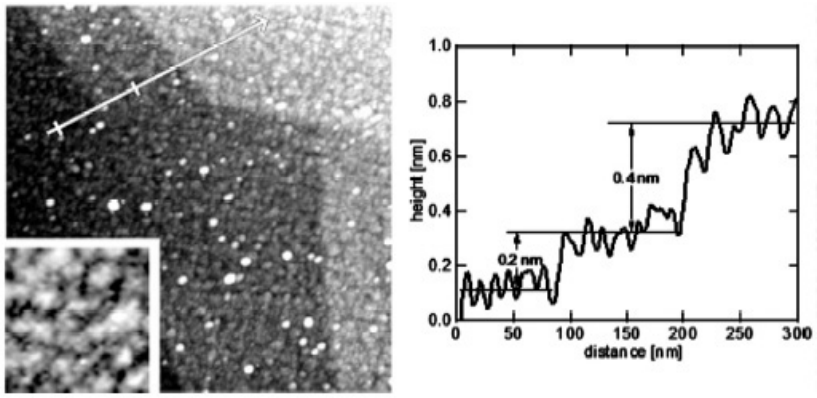

Figure 1. Left: (460 × 460) nm^2 STM image ($V = 3$ V, $I = 0.5$ nA) of 10 ML NiO film (an expanded (50 × 50) nm^2 image is shown in the inset). Right: plot of topographical heights versus position along the white line in the left panel. Reprinted from [13] with permission from Elsevier.

electron emission (PDMEE), low-energy electron diffraction (LEED) and x-ray absorption spectroscopy (XAS) all indicate that the films grow in the rock-salt structure with the O on top configuration [13, 15–17]. The films present an epitaxial strain, due to the 2% lattice mismatch with Ag, which is released above 10 ML thickness [13, 15, 17]. The interfacial distance with the Ag substrate has been measured by joint PDMEE [18–20] and XAS investigation and turned out to be 13% expanded compared to the bulk NiO interplanar distance, as also confirmed by density functional theory calculations [16]. This expanded interface may have interesting implications on the electronic properties of the very thin layers, reducing the influence of the metallic substrate in hybridization and charge screening. The film morphology for a 10 ML film is shown in figure 1 [13]. The NiO film surface shows islands of irregular shape and average diameter of 4–7 nm. The root mean square roughness is in the 0.1 nm range. Besides the features ascribed to the oxide layer, the morphology of the underlying Ag substrate, i.e. large terraces separated by monatomic or diatomic steps, can also be identified in figure 1. This indicates that the 10 ML NiO film is a good 'replica' of the substrate.

2.2. MgO

MgO is a very stable wide-bandgap material, with application as a support for metal catalysts and as an efficient protective coating material. Similarly to the case of NiO, the MgO(001) surface can also be obtained by cleavage in air, followed by UHV annealing at 400 °C for 30 min. With this procedure the surface is free of contaminants within the XPS sensitivity. Given the low lattice mismatch (3.1%) with the Ag(001) surface structure, epitaxial MgO(001) films can be obtained by growth of Mg in O_2 partial pressure on an Ag(001) single crystal. The film structure has been shown to be rock-salt by PDMEE [18–20], LEED and XAS [21, 22]. These techniques also show that at the Ag(001)/MgO interface the O-on-top configuration is the most stable. The epitaxial strain is released at 10 ML [21, 22]. A 20% expansion of the interfacial distance between Ag and MgO has been measured [22, 23]. A similar expanded value has also been predicted by *ab initio* calculations [23]. The morphology of ultrathin epitaxial MgO layers was investigated by scanning tunnelling microscopy (STM) [24]. It has been shown that at the initial deposition stage Ag atoms are partially removed from the substrate and form extended monatomic islands, leaving vacancy islands in the substrate. For submonolayer deposition, MgO condenses in the form of small islands of monatomic height,

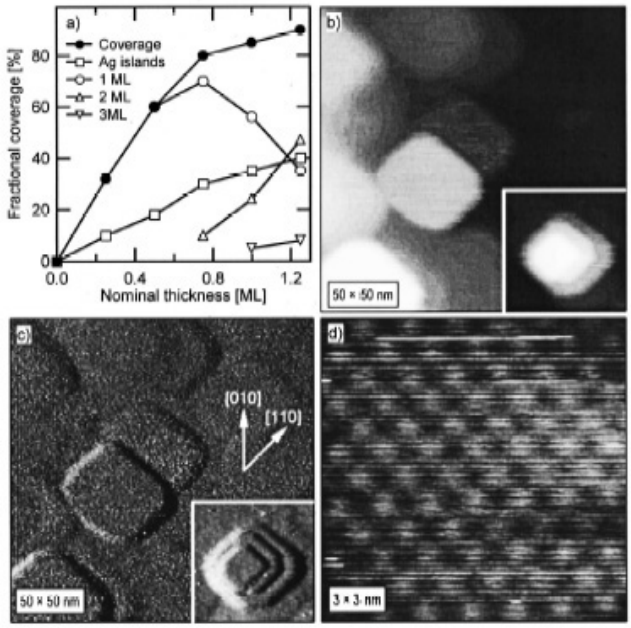

Figure 2. (a) Fraction of Ag substrate covered by Ag islands, and fraction of Ag substrate covered by MgO layer, as a function of the nominal MgO deposition; for nominal deposition of 0.75 ML or larger, the separate contributions of single and multiple MgO layers to the coverage are also shown. (b) STM image of 1 ML MgO nominal deposition (1 V, 0.3 nA). The inset shows a multilayer MgO island. (c) Current image of the same region of panel (b). (d) Atomically resolved STM image of the top layer of the pyramid of panel (b) (1 V, 0.3 nA). Reprinted from [24] with permission. Copyright (2002) by the American Physical Society.

located on the original substrate, on the protruding Ag islands and on the vacancy islands. The largest Ag(001) fractional coverage by monatomic MgO islands is 70%. A limited amount of MgO bilayers or trilayers has also been detected at this coverage. At the nominal deposition of 1 ML the formation of flat, squared and connected MgO domains of about 10 nm in width with edges along the [110] directions can be detected. The substrate fractional coverage for 1 ML MgO deposition is about 85% and the occurrence of bilayers and multilayers becomes significant (about 30% and 5% fractional coverage, respectively), resulting in the formation of three-dimensional pyramidal MgO islands. These results are summarized in figure 2. At the higher MgO coverages STM imaging becomes more difficult, due to the wide bandgap of the bulk material.

3. The Fe/NiO system

In this section we present the characterization of the Fe/NiO(001) interface, which represents a simple epitaxial ferromagnetic/antiferromagnetic system, mainly focussing on the structure and chemistry of the interface.

3.1. XPS and XPD characterization

By means of an electron beam evaporator we have deposited different amounts of Fe on a 10 ML NiO film, prepared on an Ag(001) single crystal. XPS measurements were performed

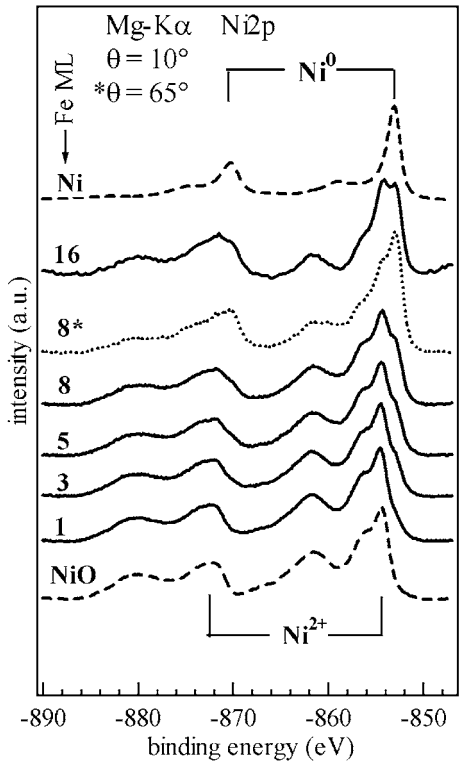

Figure 3. Ni 2p XPS spectra for the 10 ML NiO substrate (bottom curve) and for increasing Fe deposition. The 2p spectrum of pure Ni metal is shown for comparison (top curve). The spectra are collected at 10° take-off angle. For 8 ML Fe deposition, a spectrum collected at 65° take-off angle is also shown (dotted line). Reprinted from [25] with permission from Elsevier.

to investigate the composition of the Fe film and the chemical processes occurring at the interface [25, 26]. Figure 3 shows the Ni 2p spectra of the clean NiO film and after increasing Fe deposition measured at a take-off angle of 10° from surface normal. The take-off angle was integrated over ±10°, to ensure diffraction effects from the ordered substrate and overlayer to be smeared out. The Ni 2p spectrum of a pure Ni film is also shown for comparison. The substrate spectrum exhibits a bulk-like lineshape, indicating that the 10 ML NiO film is a good mimic of a bulk NiO. The deposition of Fe induces relevant changes in the substrate spectrum, reflecting the occurrence of significant modifications in the chemical bonding of the outermost substrate layers. Besides the characteristic NiO lineshape, additional features appear on the low-binding-energy (BE) side of the $2p_{1/2}$ and $2p_{3/2}$ peaks. The binding energies of such additional features correspond to that of $2p_{1/2}$ and $2p_{3/2}$ peaks in metallic Ni. The additional features become more and more intense for increasing Fe deposition, clearly indicating the occurrence of an Fe induced chemical reduction of NiO with the formation of nickel atoms in a metallic state (Ni^0), as already observed in this system [27, 28]. Changing the take-off angle from near normal to grazing, as shown in figure 3 for the 8 ML Fe case, the Ni^0 contribution to the spectrum significantly increases, indicating that the reduction process is localized in the outermost region of the substrate layer. The driving force for the NiO reduction process is expected to be the thermodynamically favourable Fe oxidation with respect to Ni oxidation, due to the higher oxygen affinity of Fe. Therefore, concurrent with NiO substrate reduction,

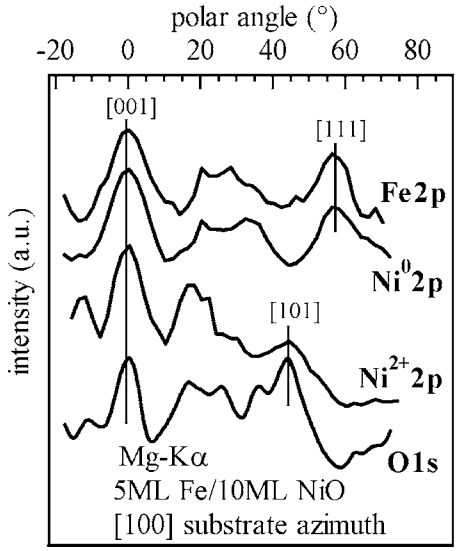

Figure 4. Intensity distribution of the Ni^{2+} and Ni^0 2p, O 1s and Fe 2p as a function of the polar take-off angle along the [100] substrate azimuth, for 5 ML Fe/NiO. The spectra have been normalized to the intensity of the [001] peak. Reprinted from [25] with permission from Elsevier.

oxidized states are observed for the metal overlayer. In fact, in the Fe 2p photoemission spectra recorded at the low deposition stage (not shown here), additional intensity appears on the lower-BE side of metallic Fe spectra [25]. This contribution can be ascribed to the presence of Fe atoms in an Fe^{2+} state on the basis of the lineshape of the difference spectrum [29]. The extent of the observed interfacial oxidation–reduction reaction can be quantified, considering the morphology of the system. It has been shown by STM that Fe forms islands of 2–3 nm lateral dimension for coverages up to 5 ML [26]. This growth mode is expected to greatly affect a quantification of the reaction simply based on the evaluation of the relative weight of Ni^{2+} and Ni^0 components of the Ni 2p spectra. In fact, the reduction process only involves the fraction of the substrate covered by Fe islands. Possible Fe–Ni alloying at the interface should also be taken into account, as described in the following.

Information on the interface morphology and species distribution have been obtained by x-ray photoelectron diffraction (XPD) measurements, which allowed us to determine the chemically resolved local environment of the different atomic species in the growing film and in the interfacial region. Polar scans with an angular resolution of $\pm 1^\circ$ along the [100] substrate azimuth on the (001) surface of the NiO film were measured by rotating the sample in front of the analyser by steps of 2°. The intensity angular distribution (IAD) of Fe 2p, O 1s and the chemically resolved Ni^{2+} and Ni^0 components of the Ni 2p spectrum are shown in figure 4. The O 1s and Ni^{2+} 2p IADs are very similar, both reflecting the symmetry of the rock-salt structure of the NiO substrate along the selected [100] azimuth. In contrast, the metallic Ni signal intensity oscillates in strict agreement with the Fe signal intensity, indicating a body centred tetragonal (bct) local atomic environment for the interfacial metallic Ni. This suggests the formation of a bct Ni–Fe alloy at the interface. The possible formation of an M–Ni (M = Fe, Co) alloy has been mentioned by other authors [28, 30]; however, all of the previous quantitative models for the interface assumed the reduced Ni atoms to remain confined in the substrate topmost region without giving details of their structure. The XPD results of figure 4 on the contrary suggest that some degree of Fe–Ni intermixing actually occurs and must be

included in the interface modelling for a reliable quantification of the oxidation–reduction process. We assumed this alloy to have an average Ni concentration of 25% (the maximum Ni concentration for which bulk Fe–Ni alloys are stable in a bcc structure). The strength of the oscillations in the Fe and Ni^0 IAD also gives information on the overlayer growth mode, which has to be taken into account in the quantification of the reduction process. In order to explain the discrepancies between the measured and calculated (multiple scattering based simulations [31]) anisotropy values, three-dimensional island Fe growth has also to be called into play. For 1 ML deposition the measured XPD anisotropy suggests that the alloy aggregates in 2.6 ML thick islands covering 50% of the substrate. A complete NiO surface coverage is only obtained for 5 ML Fe deposition. Based on this model and on the intensity of the Ni^{2+} and Ni^0 components of the Ni 2p XPS spectrum as a function of Fe deposition, we found that the amount of NiO affected by the reduction process increases with the amount of deposited Fe, while the reduction rate decreases. The process stops for Fe deposition larger than 5 ML, when the surface coverage is complete, indicating that the strength of the interfacial reactions is controlled by the uncovered fraction of the NiO surface. The discrepancy in the number of reduced NiO layers with respect to results reported by other authors [28] is possibly ascribable to the simplified model they used, where the alloy formation and the islanding growth mode were not included. It is noticeable that, in spite of the complex interface, the formation of an epitaxial and well ordered Fe overlayer is observed. The interfacial intermixed Fe–Ni bcc phase formed as a consequence of the NiO reduction process, promoted by Fe atom deposition, is expected to have a significant influence on the magnetic couplings and has to be taken into account to calculate the magnetic properties of this system. Both the Curie temperature and the magnetic moment of the ferromagnetic overlayer are expected to become lower as the interfacial intermixing occurs, due to the decrease of Fe concentration in the Fe film [30, 32]. The presence of Fe–O aggregates in the overlayer may also have relevant consequences on the magnetic couplings, which are expected to strongly depend on the location of O atoms within the Fe film. It is difficult, however, to answer to this question by XPD, since other spectral contributions lie in the kinetic energy region of the low-intensity oxide component. The separation of metallic and oxidized Fe components is therefore a very challenging task. The characterization of the Fe local atomic environment was performed by XAS, as reported in the following.

3.2. XAS characterization

The Fe K-edge XAS characterization was performed at the GILDA beamline of the European Synchrotron Radiation Facility [33]. We exploited the polarization dependence of the XAS cross section by changing the relative orientation between the sample normal and the polarization of the impinging x-ray beam in order to preferentially probe either the in-plane or out-of-plane atomic correlations. Data analysis was performed by the standard software package UWXAS [34], using the theoretical scattering amplitudes and phase shifts generated by the FEFF8.10 code [35] for the fitting. The background subtracted extended x-ray absorption fine structure (EXAFS) spectra in the two geometries for a 2 ML Fe film grown on NiO(001) are shown in figure 5(a). Figure 5(b) shows the corresponding magnitude of the Fourier transforms and the results of structural fits in which the coordination numbers, the interatomic distances and the Debye–Waller factors were fitting parameters. The inset of figure 5(b) shows the details of the near-edge region of the XAS spectra in the two experimental geometries. The near-edge spectrum measured at 75°, i.e. in a configuration more sensitive to in-plane atomic correlations, has a higher ratio between the intensity of the white line and the intensity of higher-energy structures than the 15° spectrum and closely resembles the spectrum of bulk FeO (not shown).

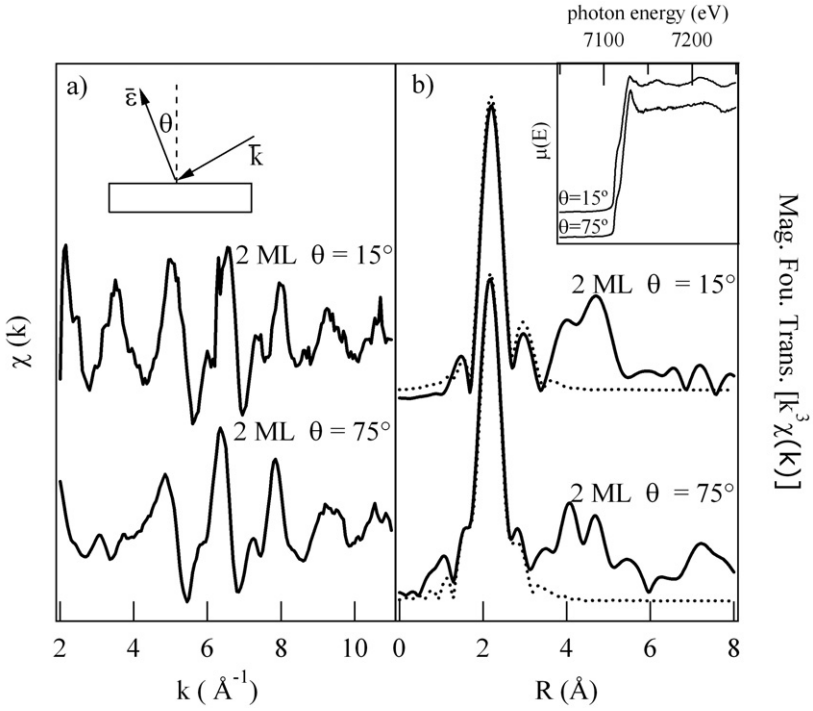

Figure 5. (a) Background subtracted Fe K-edge EXAFS spectra for the 2 ML Fe film in the two geometries. (b) Corresponding $k3$ weighted magnitude of the Fourier transforms (solid line) and fit (dashed line). Inset: Fe K-edge near-edge XAS spectra in the two geometries. Reprinted from [6] with permission. Copyright (2006) by the American Physical Society.

This is a clear indication of a preferential formation of Fe–O coordinations in the film plane. The fitting of the extended range spectra was therefore performed assuming the formation of a planar FeO-like layer. The Fe–O distances resulting from the fit are much larger out of the film plane (2.38 ± 0.07 Å) than in the film plane (2.07 ± 0.07 Å). It is impossible from the XAS data alone to determine whether the FeO layer is between the NiO substrate and the Fe layer or on top of the metallic film; however, in the following we shall consider the former hypothesis (see model in figure 6), based also on the considerations derived by the *ab initio* calculations reported below. Assuming this model, the FeO-like layer exhibits a 0.29 ± 0.14 Å buckling, with O and Fe atoms respectively shifted towards and away from the underlying NiO substrate. Moreover, the distance between the last NiO plane and the average position of the FeO plane is 2.24 Å, a value 7% larger than the interplanar distance of bulk NiO. A body-centred-tetragonal (bct) Fe–Ni phase is present on top of the interfacial FeO layer.

The DFT calculations of the Fe/NiO(100) interface have been performed by means of the all-electron linearized augmented plane wave (LAPW) method [36, 37] as implemented in its newest version, e.g. APW + local orbital (APW + lo) [38, 39], in the WIEN2k package [40]. Because of the hybrid nature of the basis set used, the APW + lo method is one of the most accurate approaches for the study of transition metal compounds. The exchange and correlation potential is considered in the generalized gradient approximation (GGA) proposed by Perdew, Burke and Ernzerhof (PBE) [41]. A slab calculation, in which two monolayers of an $Fe_{0.5}Ni_{0.5}$ alloy are adsorbed on each side of five-layer-thick NiO slabs in the presence of an FeO interface layer, indicates that the preferred adsorption site for Fe is on top of the oxygen

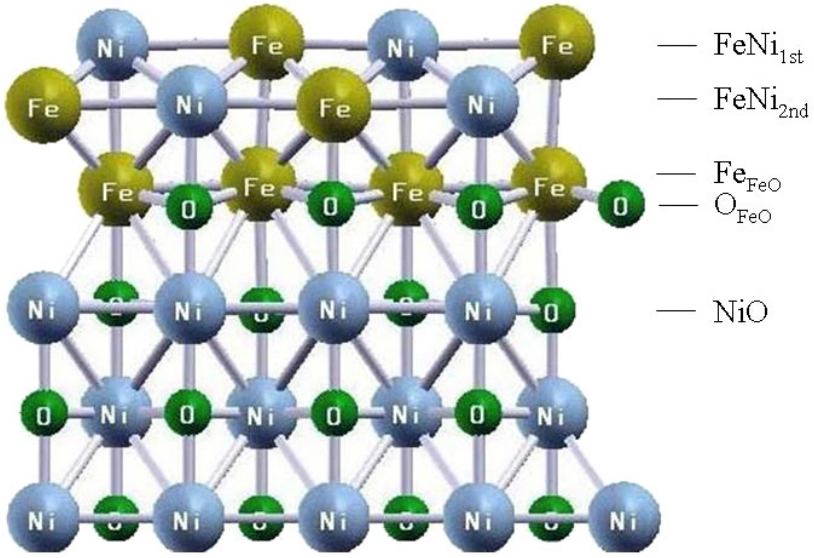

Figure 6. Relaxed interface structure of 2 ML FeNi on NiO, with an FeO interface layer, as calculated by DFT; the values of the interlayer distances are given in table I in [6] (picture generated by XCrySDen [105]). Reprinted from [6] with permission. Copyright (2006) by the American Physical Society.

atoms in the NiO interface layer. The bulk AF2-type antiferromagnetic ordering between the Ni magnetic moments has been assumed for the NiO + FeO slab. The structurally relaxed atomic configuration for Fe/NiO(001) is depicted in figure 6. We observe moderate deviations of the interlayer distances in the NiO layers, which are always close to the bulk interlayer distance of 2.08 Å. The Fe atoms, in contrast, relax outwards with respect to oxygen atoms in the FeO interface layer. The average Fe–O out-of-plane distance at the interface is found to be 2.42 Å, with a buckling between the Fe and O atoms in the FeO interface layer of 0.34 Å. A contraction to 1.88 Å is found in the distance between Fe atoms in FeO and the lowest FeNi alloy layer. The overall experimental and theoretical structures compare very well. In particular, there is a very good numerical agreement in the values found for the buckling of the FeO layer and for the expanded distance between the FeO layer and the underlying NiO. The differences for some of the interatomic distances, in particular the one between the FeO-like layer and the overlying metal, may be due to the fact that XAS sees an average of the distances actually present in the sample.

The calculations also allowed us to evaluate the spin magnetic moment of the Fe atoms at the interface. We compared the values obtained assuming the presence of a pure, pseudomorphic, Fe layer and the formation of an oxidized FeO layer. A significant increase by approximately 0.6 μ_B (from 2.6 to 3.2 μ_B) in the distorted FeO layer was found. The origin of this change lies in a depopulation of minority spin d orbitals involved in the Fe–O bonds. The Fe atoms of the interfacial FeO layer assumed in our model are in fact more coordinated with oxygen atoms than Fe atoms situated in the first layer of the ideal Fe/NiO interface, therefore a higher spin polarization is achieved. This is in agreement with calculations by Chubb and Pickett [42], which predict an increase in the Fe surface moments upon adsorption of oxygen atoms. Uncompensated moments coming from the interfacial FeO layer, which may couple ferromagnetically with the Fe layer, are expected to influence dramatically the

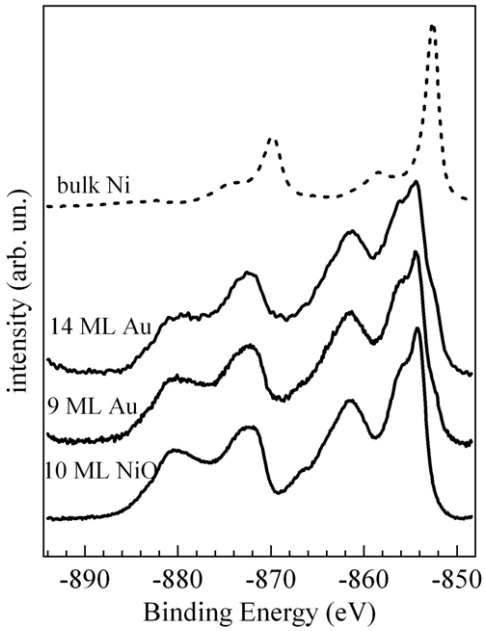

Figure 7. Ni 2p XPS spectra of a bare 10 ML NiO film on Ag(100) and after 9 and 14 ML Au deposition. The bulk Ni 2p reference (dashed line) is also shown. The spectra are measured with a 65° take-off angle.

exchange interaction at the Fe/NiO interface, with deep consequences also for the exchange bias mechanism.

A magnetic characterization of the system by means of the magneto-optical Kerr effect (MOKE) and other techniques is currently running, to obtain the experimental evaluation of the predicted magnetic properties.

4. The Au/NiO system

In order to investigate the dependence of NiO interfacial reactions on the oxygen affinity of the metal deposit, we also studied the Au/NiO interface. Also in this case, in fact, the reduction of a small fraction of NiO was previously observed, although the reasons for and the details of this effect have not been discussed exhaustively [27].

We performed XPS measurements on Au films of different thicknesses deposited at room temperature on a 10 ML NiO film on Ag(100). Figure 7 shows the Ni 2p spectra measured at 65° take-off angle for clean NiO and for increasing Au amount. After Au deposition the spectra show a shoulder on the low-binding-energy side of the Ni^{2+} $2p_{3/2}$ peak, corresponding to the formation of metallic Ni. The relative intensity of metallic and oxidized components increases as a function of Au thickness. The presence of the metallic shoulder in the XPS spectra is a clear indication that the deposition of non-reactive Au atoms also induces to some extent the reduction of NiO. From the analysis of Ni^0, Ni^{2+} and Au 4f intensities as a function of Au amount and take-off angle, the following model emerged [43]: the reduction of NiO is rather limited (∼0.3 ML) and occurs at the very early stages of Au growth. The metallic Ni atoms however do not remain confined at the interface between Au and NiO, but they are diluted into the Au layer. The possibility of having metallic Ni atoms located at the surface of the Au layer, rather unlikely if one considers the Ni and Au surface free energies (1.94 and 1.41 J m^{-2} respectively [44]), has been definitely ruled out by the fact that the exposure of the 9 ML Au/NiO sample to 5 L of O_2 did not give rise to any change in the relative weight

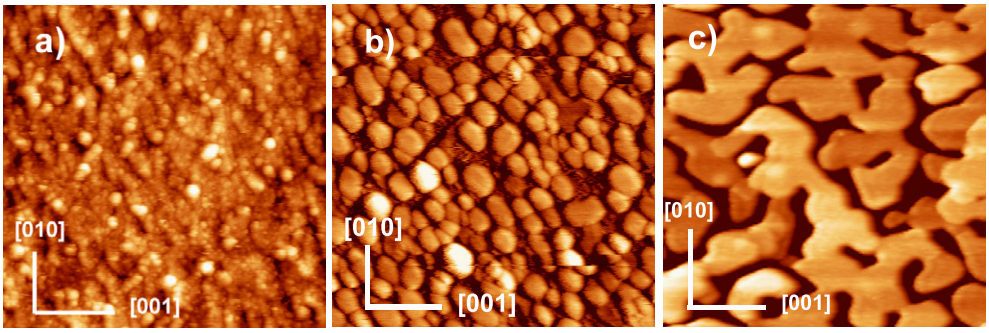

Figure 8. (200 × 200) nm^2 constant current topographic STM images of (a) a bare 7 ML NiO film on Ag(001) ($I = 0.02$ nA, $V = 3$ V), (b) 1 ML Au ($I = 0.3$ nA, $V = 2$ V) and (c) 9 ML Au ($I = 0.1$ nA, $V = 0.5$ V) deposited on it.

of Ni^0 and Ni^{2+} components in the photoemission spectrum. Au and Ni are immiscible at room temperature [45]; nevertheless, in ultrathin layers deviations from the bulk behaviour are frequent and alloying phenomena at the Au/Ni(110) interface have already been observed [46]. This supports our conclusion that the metallic Ni can be diluted into the Au clusters.

We also investigated the influence of the growth rate on the Au induced NiO reduction by changing its value in the 1–0.15 Å min^{-1} range. Low evaporation rates have been found to favour the reduction, suggesting that kinetics plays a role in the process. NiO reduction, instead, is lower than the XPS sensitivity if Au is evaporated onto a NiO single crystal, suggesting that the roughness of the NiO film, and the consequent high density of low coordination sites at the surface, is responsible for the unusual chemical activity at the Au/NiO interface.

In order to investigate the morphology of Au on NiO we performed STM measurements on a 1 and 9 ML nominal Au deposition on a 7 ML thick NiO film grown on Ag(001). The instrument has been operated in constant current mode with low current values (∼0.1 nA). The NiO film presents a surface with small round clusters of 4 nm average width and 0.5 to 2 nm height (figure 8(a)). After 1 ML of Au deposition we observe the presence of large Au islands (figure 8(b)). The width of the Au islands is between 8 and 20 nm and their average height is about 2 nm. In this image the fraction of uncovered NiO (the darker areas in which smaller clusters are visible) is approximately 20%. It has to be noted that the Au cluster height can be an artefact induced by the different electronic structures of Au and NiO. After the deposition of the first layer, Au grows in a 3D mode, as shown in figure 8(c) obtained on a 9 ML Au sample. The Au clusters have a worm-like shape with lateral dimensions ranging from 15 to 90 nm and a height of 3–5 nm. The fraction of NiO surface covered by Au clusters is unaltered from 1 to 9 ML of nominal Au deposition.

5. The Fe/MgO system

The interest in the preparation and characterization of Fe layers on MgO has increased in recent years owing to their technological applications in catalysis [47], electron spin polarimetry [48], epitaxy [49, 50] and magnetic recording [51–53]. Fe on MgO also represents a model system to investigate the transition between 2D and 3D growth in thin films [54]. The importance of the quality of the interfaces for the performances of alternating layers with different magnetic properties and thickness in the nanometre range has been widely recognized [5, 8, 9]. The variety of procedures used for MgO substrate preparation and for Fe deposition leads to

different growth modes, morphologies and crystalline qualities of the Fe layers and of the Fe/MgO interface [55–59].

The aim of this section is to report on the growth mode, the structure, the interface chemistry and the stability versus temperature of 1–10 ML Fe films deposited on a cleaved MgO(001) surface, in the RT–500 °C temperature range [60, 61]. The procedures for substrate preparation and Fe deposition were very similar to the Fe/NiO(001) case. Structural analysis has been performed by PDMEE [18–20] and LEED. XPS was used to obtain a first indication of the chemistry and the growth mode of the interface. XAS was used to investigate the chemical state of Mg and Fe atoms.

5.1. Structure and interface

In a typical PDMEE experiment, the Auger intensity angular distribution (IAD) is recorded as a function of the beam incidence angle, scanned by tilting the sample around definite directions. Auger measurements were detected in the first derivative mode by a cylindrical mirror analyser (CMA) operating at 0.6% resolution and 15 V modulation. The coaxial gun was operated at 1.2 keV and 1 μA beam current.

On the clean MgO(001) surface, the O KLL Auger peak was recorded as a function of the incidence polar angle along the [100] and [110] azimuthal directions (figure 9, curve (a)). On the 10 ML Fe/MgO system, the Fe LVV Auger peak was monitored as a function of the incidence angle, for different deposition temperatures and post-deposition annealing temperatures (figure 9, curves (b)–(e)). The Fe LVV signal intensity from the (001) surface of an Fe single crystal prepared by repeated cycles of sputter-annealing was measured, as it provides a reference curve for the bcc structure (figure 9, curve (f)). The IAD of the O KLL Auger peak from the clean MgO substrate shows the typical features of a cubic structure. Two main peaks appear at 0° and 54.7° along the [110] azimuth, corresponding to the forward focusing of the primary beam along the $[00\bar{1}]$ and $[\bar{1}\bar{1}\bar{1}]$ crystalline directions, respectively. Along the [100] azimuth, forward focusing peaks occur at 0° and 45°, in correspondence to the $[00\bar{1}]$ and $[\bar{1}0\bar{1}]$ crystalline directions, respectively. Other features are mainly generated by interference between the scattered waves [62]. The Fe LVV IAD from the 10 ML Fe deposited at RT (figure 9, curve (b)) clearly indicates the formation of a bct layer with a (001)Fe ∥ (001)MgO and [110]Fe ∥ [100]MgO orientation relationship with the substrate, in agreement with previous findings [54, 55, 58, 57, 63, 64]. The side of bcc Fe can easily in fact match the diagonal of the MgO rock-salt structure with a small expansive strain (3.8% mismatch). The 10 ML Fe film IAD features on both substrate azimuths closely resemble those detected in the bulk Fe IAD (figure 9(f)). The tetragonal distortion of the film along the growth axis is suggested by the angular shift of the $[\bar{1}0\bar{1}]$ and $[\bar{1}\bar{1}\bar{1}]$ peaks in the IAD (by $+1.6°$ and $+1.4°$ respectively) with respect to peaks on the Fe crystal.

The Fe LVV/Mg KLL and O KLL/Mg KLL Auger intensity ratios are shown in figure 10 for 10 ML Fe on MgO, deposited at RT and annealed at increasing temperature. In figure 10(a) the experimental data (symbols) are compared to the results of a simple exponential attenuation model in which part of the substrate is left uncovered. The fractional coverage has been considered as the only independent variable which determines the Auger intensity ratios in figure 10(a). The Fe LVV/Mg KLL Auger intensity ratio (figure 10(a)) suggests that the 10 ML Fe deposited at RT are organized in a nearly continuous layer (90% fractional coverage, figure 10(b)). This is also consistent with the observed reduction of the O KLL/Mg KLL intensity ratio with respect to the clean MgO surface (from 3.5 to 2.3, figure 10(a)). The formation of a continuous film for 10 ML RT deposition is in agreement with previous findings [51, 56, 59]. The substrate fractional coverage and the tetragonal distortion of the

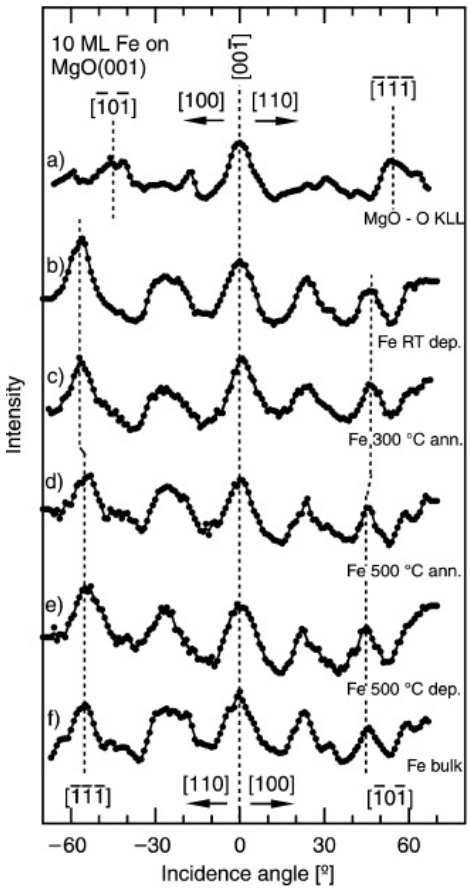

Figure 9. Intensity distribution of O KLL and Fe LVV Auger electrons versus the incidence angle of the electron beam along the [1 0 0] and [1 1 0] azimuths on the clean (0 0 1) surface of MgO and Fe single crystals, and on the 10 ML Fe film for different deposition and/or annealing conditions. From top to bottom: (a) O KLL on the clean MgO substrate; (b) Fe LVV on the RT deposited Fe film; (c) Fe LVV on the film deposited at RT and annealed at 300 °C; (d) Fe LVV on the film deposited at RT and annealed at 500°C; (e) Fe LVV on the film deposited at 500 °C and (f) Fe LVV on the Fe single crystal. Reprinted from [60] with permission from Elsevier.

Fe bcc lattice is not substantially affected by annealing the film up to 300 °C. A reduction of the coverage from 90% to 75% is observed at 400 °C. At 500 °C the O KLL/Mg KLL intensity ratio reaches the same value as measured on the clean MgO surface. A fractional coverage of 35% is evaluated by the Fe LVV/Mg KLL intensity ratio at 500 °C (figure 10(b)).

From the structural point of view, annealing at 500 °C completely removes the tetragonal distortion and forces the RT deposited layer to assume the ideal bcc structure. 10 ML thick Fe layers deposited on the MgO substrate held at 500 °C show the same bcc structure but a larger fractional coverage (52%) with respect to the 500 °C annealed film.

The Fe IAD at 500 °C well reproduces the shape and anisotropy of the distribution the IAD of an Fe single crystal, indicating that the Fe atoms have a local bcc atomic environment. In addition, the peak splitting typical of Fe in an oxidized state [65] was not observed in the Fe MVV Auger peak lineshape, as shown in the inset of figure 10.

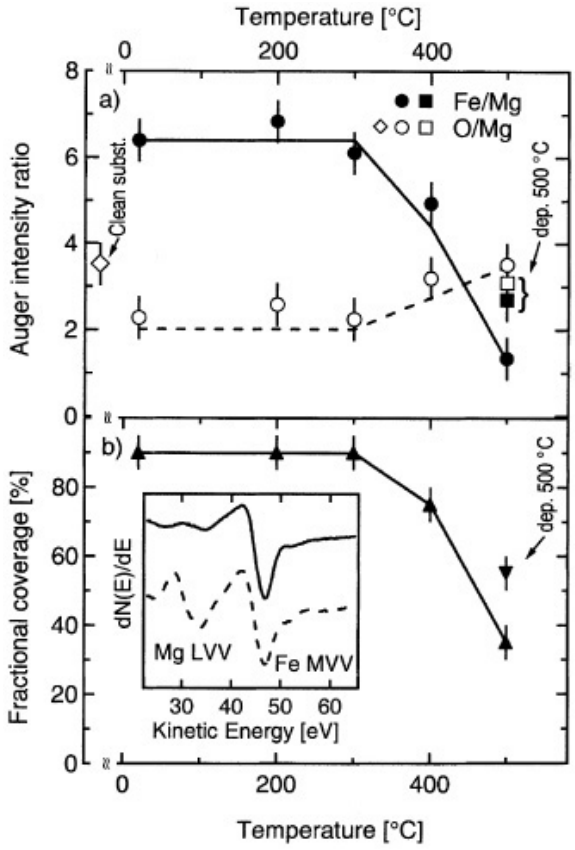

Figure 10. (a) Fe LVV/Mg KLL (●) and O KLL/Mg KLL (○) Auger intensity ratios for 10 ML Fe on MgO, deposited at RT and annealed at increasing temperatures. The O KLL/Mg KLL ratio for the clean MgO substrate is also shown. The lines are the result of a calculation of the intensity ratios based on an exponential intensity attenuation model assuming the fractional coverage as a fitting parameter. The output of such a modelling is shown in (b), where the fractional coverage of the MgO substrate for 10 ML Fe deposition at RT and subsequent annealing at increasing temperature is reported. Auger intensity ratios (□, ■) and fractional coverage (▼) for the 500 °C deposited film are also shown. The inset shows the Fe MVV Auger lineshape for the RT deposited (——) and 500 °C annealed (- - - -) Fe film. Reprinted from [60] with permission from Elsevier.

LEED and secondary electron imaging (SEI) analysis [66, 67] has been performed by a rear-view, four-grid apparatus. Diffraction patterns were recorded using a cooled, 16-bit CCD camera. LEED patterns are rather diffuse and present a fourfold symmetry, rotated by 45° with respect to the substrate. As the temperature increased, the LEED pattern became sharper. SEI plots are the stereographic projection of the intensity of backscattered electrons with respect to the polar and azimuthal escape angles. The main features in the intensity distribution are related to the forward focusing of inelastically backscattered electrons escaping along the most closely packed, crystalline atomic chains [68]. This method therefore probes the real-space crystal structure of the near-surface region [66, 67]. SEI patterns confirm that the RT deposited Fe film has a bcc-like structure, with main axes rotated by 45° with respect to those of the substrate. Owing to the chemical insensitivity of the SEI signal, and to the occurrence of Fe islanding at high temperature, the SEI pattern of the Fe layer deposited at 500 °C is expected to reflect the symmetry of both the Fe film and the uncovered substrate. Assuming the pattern to be roughly a

linear superposition of the substrate and Fe patterns, it has therefore been reproduced by a linear combination of these reference patterns, weighted by the different backscattering efficiencies of Fe and MgO, using the fractional coverage as fitting parameter. A best fit procedure leads to a fractional coverage of 56%, in good agreement with the 52% value deduced from the Auger intensity ratios (figure 10).

In spite of the huge number of studies on the Fe/MgO(001) system, the interface properties are rarely taken into consideration [69]. Concerning interfacial chemical interactions, it should be considered that the heat of formation of MgO is more negative than that of the most stable Fe oxide [70], therefore thermodynamics does not predict the occurrence of an oxidation–reduction reaction at the Fe/MgO interface. However, at the opposite interface, MgO/Fe(001), Meyerhiem *et al* observed the formation of an FeO layer [71, 72].

We used XPS and XAS to obtain a first indication of the structure and the chemistry of the Fe/MgO(001) interface. XPS analysis of Fe films of increasing thickness (1–10 ML) was performed using Al Kα photons as the exciting source. The measurements were performed using a non-monochromatized x-ray source and a hemispherical analyser operating at a normal take-off angle. No evidence for MgO reduction was detected in the Mg 1s spectra. Fe 2p 3 and 1 ML spectra show a slight broadening of the $2p_{3/2}$ peak towards higher binding energies, possibly ascribed to a contribution by oxidized Fe atoms, whose 2p photoelectrons are expected to have a higher binding energy [29]; broadening can also be due to the correlation satellites observed in core level photoemission lines when the dimensionality of the systems is reduced [73]. The XPS measurements therefore are not conclusive concerning the chemistry of the interface.

In order to have a definite and reliable picture of the Fe/MgO(001) interface, we measured x-ray absorption spectra on the Mg K edge and Fe L edges of Fe/MgO samples. In this case we expect remarkable differences in the Fe and Mg XAS lineshapes in samples with different oxidation states and local environments, as reported in the literature [22, 28]. Fe L-edge and Mg K-edge XAS measurements were performed at the BEAR beamline [74] of the ELETTRA synchrotron radiation facility. The geometry used for XAS measurements was with the photon beam at 45° from the sample normal and the electric field in the growth plane. The spectra were collected in drain current mode without any bias applied to the sample.

Mg K-edge spectra for the MgO clean substrate and after the growth of Fe films of increasing thickness in the 0.7–10 ML range are very similar (figure 11(a)). However, the presence of a fraction of reduced MgO at the interface layers may be too small to give marked changes in the 10 ML MgO spectra. Figure 11(b) shows Fe L-edge XAS measurements of the Fe films of different thickness, in comparison with a bulk Fe spectrum taken from [28]. The 10, 2 and 1.4 ML films have a bulklike lineshape with the same energy positions and width of the L_3 and L_2 peaks. The search for interfaces which are stable in temperature is also a crucial aspect. Figure 12 reports the spectrum of the as grown 1.4 ML sample, the spectrum obtained after heating the sample up to 670 K and the one after exposing it to 10^3 L of O_2 (assumed to be the saturation exposure) at 400 °C. The difference between the as-grown spectrum and the one measured after heating is within the noise level. A clear narrowing and shift to 1.7 eV higher photon energy of the L_3 peak can be detected after high temperature oxygen exposure of the sample. The L_2 edge is broadened and shifted to higher photon energy, in agreement with the formation of an Fe oxide film after the high-temperature oxygen exposure, as can be seen by comparison with the spectra from Fe_3O_4 and Fe_2O_3 samples (taken from [28]). If a part of the 'as-grown' film were oxidized to Fe_3O_4 or Fe_2O_3, we would expect a shoulder in the L_3 peak at approximately 1.7 eV higher binding energy. This demonstrates that the Fe/MgO interface, as predicted theoretically [75], is non-interacting and stable up to temperatures higher than normal device operation ones.

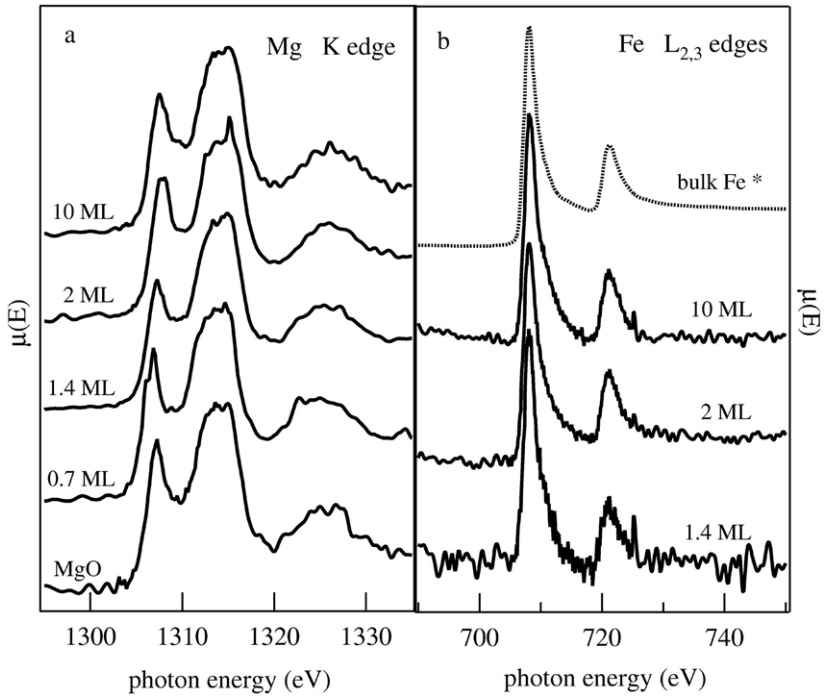

Figure 11. (a) Mg K-edge XAS spectra of the clean MgO substrate and after the growth of Fe films of different thickness. (b) Fe $L_{2,3}$-edge XAS spectra of Fe films of different thickness and of a bulk metallic Fe (dashed line, taken from [28]). Reprinted from [61] with permission from Elsevier.

5.2. Magnetic properties at the nanoscale

A significant amount of experimental and theoretical work has been done by the scientific community over recent years to address different aspects of ordered magnetic micro-nanostructures, from fabrication to characterization. Many of the interesting phenomena of such systems come about by imposing a spatial confinement [76–80], which is comparable in size to some internal length scale of the material used. For instance, the magnetostatic energy associated with the lateral confinement is known to induce a dependence of the magnet free energy on the magnetization direction (magnetic anisotropy) in nearly single-domain elements [76]. The anisotropy of small magnetic elements can be controlled to a large extent by imposing a suitable shape. This allows the engineering of the so-called 'shape anisotropy' [76], that for a non-uniform magnetization state conventionally includes the 'true' shape anisotropy (i.e. the anisotropy of the magnet in the uniform magnetization state) and a correction term called 'configurational anisotropy' [81–83], which accounts for the energy difference between the uniform and the actual magnetization state of the magnet. The shape and configurational anisotropies, together with the intrinsic magnetocrystalline anisotropy (if any) determine the total anisotropy of the magnet.

To study the interplay between all these contributions in Fe micro and sub-micro magnets, we fabricated by focused ion beam (FIB) milling a set of arrays of single-crystal Fe elements on MgO [84, 85]. FIB is a versatile nanofabrication tool based on the interaction of nanosize beams of energetic Ga ions with solid surfaces [86–88]. With respect to state-of-the-art lithographic technologies, FIB offers a comparable resolution (a few tens of nanometres)

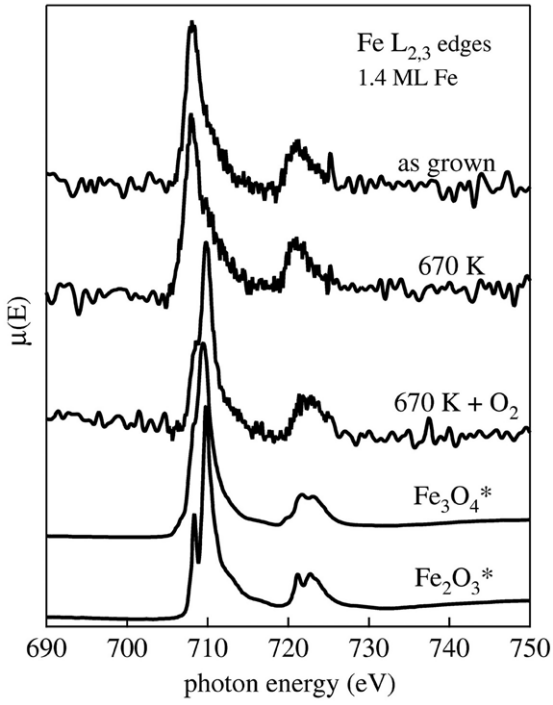

Figure 12. Fe $L_{2,3}$ XAS spectra of a 1.4 ML Fe film after growth, after heating to 670 K and after heating to 670 K during exposure to an oxygen dose of 10^3 L. The figure also shows the Fe $L_{2,3}$ XAS spectra of an Fe_3O_4 and an Fe_2O_3 sample (taken from [28]) for comparison. Reprinted from [61] with permission from Elsevier.

with higher flexibility, enabling one-step maskless etching. Etching occurs by physical ion sputtering [84, 89, 90], optionally gas assisted to enhanced material removal rates or species selectivity [91].

Single-crystal, 10 nm thick Fe films have been grown on freshly cleaved MgO(001) substrates by molecular beam epitaxy (MBE). To avoid oxidation, the Fe film has been capped with a 10 nm thick MgO layer, deposited by reactive MBE from the elemental precursors. FIB has been subsequently used to selectively remove portions of the film to produce the different arrays. The samples were milled to a depth sufficient to completely remove the MgO/Fe bilayer. Figure 13 shows scanning electron microscopy (SEM) images of portions of the patterned regions. The interdot distance is large enough to have negligible magnetostatic interaction between the nanomagnets.

The samples were magnetically characterized using a magneto-optical Kerr microscope/magnetometer (μMOKE) measuring the longitudinal Kerr effect [92]. The easy- and hard-axis μMOKE loops of the film are shown on the left-hand side of figure 14. No out-of-plane component of the magnetization has been found, as expected for thick Fe layers. The coercive field ($\approx$20 Oe) measured in the easy-axis loop is small compared to the hard-axis saturation field ($>$500 Oe), indicating that the magnetization reversal is determined by nucleation and expansion of reversed domains, as already observed for thin single-crystal Fe films [93].

Let us now consider the patterned structures. The diagonals of the square elements are parallel to the film easy axes. At first order, the configurational anisotropy in square nanomagnets of this size and thickness (both patterns 1 and 2) was found to have an in-plane fourfold symmetry with easy directions along the square diagonals [82]. The easy axes for configurational anisotropy being coincident with those of intrinsic magnetocrystalline anisotropy [81–83], the symmetry of the overall anisotropy of the square nanomagnets should be the same as in the continuous film. The same symmetry is expected for the circular

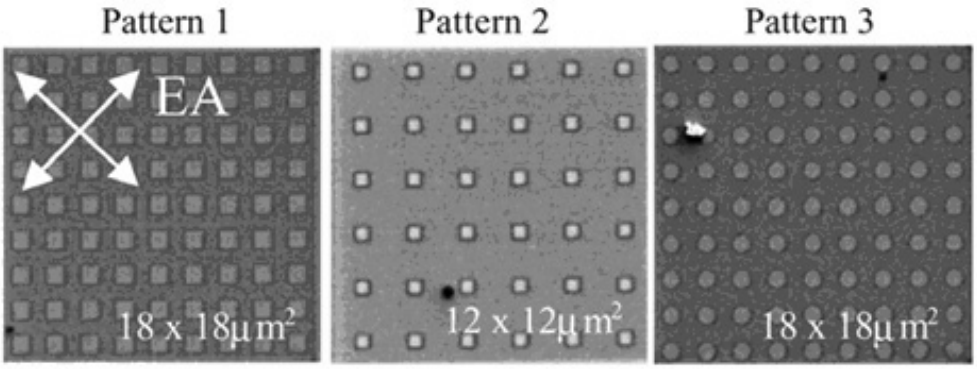

Figure 13. Scanning electron microscopy images of portions of the patterned areas. Pattern 1 is an array (pitch of 2 μm) of square elements of 1 μm side; in pattern 2 the lateral size of the square elements is reduced to 500 nm; pattern 3 is an array of circular elements of 1 μm diameter. The white arrows indicate the direction of the magnetocrystalline easy axes of the film. Reprinted from [84], with permission from Elsevier.

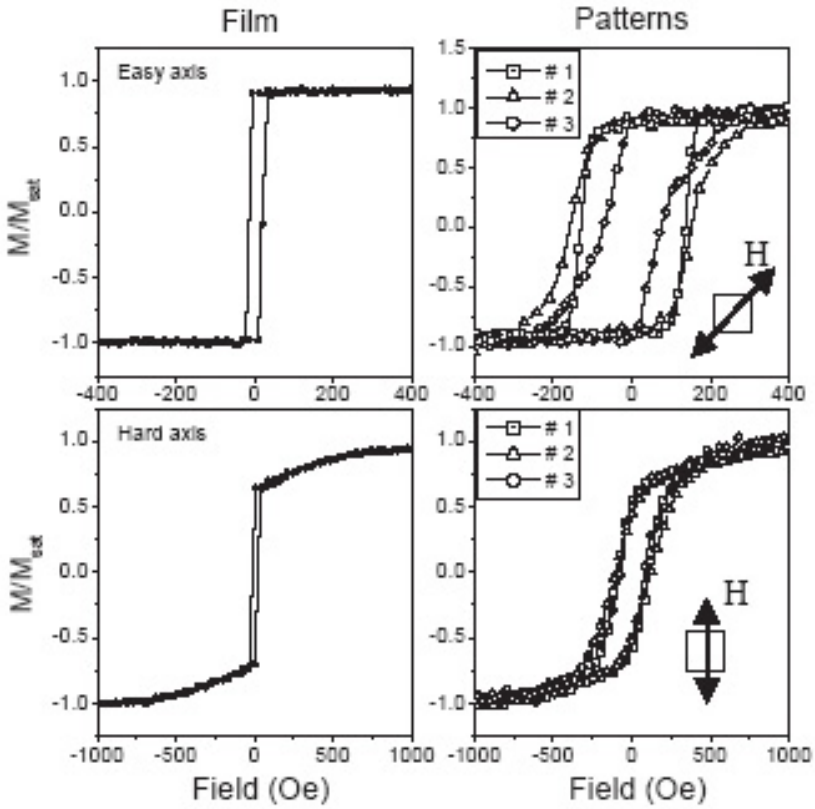

Figure 14. Left-hand side, μMOKE hard- and easy-axis hysteresis loops for the Fe film; right-hand side, μMOKE loops measured from the patterned areas, applying the external field along the same directions as for the continuous film. Reprinted from [84], with permission from Elsevier.

nanomagnets of pattern 3, because the magnetic in-plane configurations are energetically isotropic (i.e. there is no configurational anisotropy). This is confirmed by the hysteresis loops shown on the right-hand side of figure 14, which show that the easy and hard magnetization directions of the film and the structures are coincident. However, the hysteresis loops of the patterned areas are very different if compared to that of the continuous film in both the shape and the coercive field. Micromagnetic simulations [94], not shown here, point out that these differences are determined by the lateral confinement, which hinders domains formation during the magnetization reversal. As a result, the nucleation of magnetization reversal is retarded, the coercive field is increased with respect to the continuous film and the magnetization switching takes place more gradually.

The easy-axis loops show peculiar differences for the different patterns. First, the nucleation field for magnetization reversal is much higher for the square elements than for the circular ones. In square elements, the magnetization switches between two reversed 'leaf' states [83]. For circular elements of this size, the magnetization is expected to switch between two reversed S-shaped configurations [95]. The lower stability (higher energy) of the 'S' state with respect to the 'leaf' one, confirmed by numerical simulations, explains the lower nucleation field observed for circular elements. Concerning differences between square patterns, the hysteresis loop for the 500 nm dots is more sheared and smoother than that of the 1 μm dots. This suggests that the diagonal becomes a 'less easy' direction upon reducing the lateral size of a square magnet. This is because the configurational anisotropy in a square magnet is only at first order fourfold symmetric [83]. This is confirmed by numerical simulations, which show a high-order term with eightfold symmetry [81], which increases as the lateral size of the element is reduced.

Regular arrays of micrometric circular Fe dots (width 2.5 μm, height 300 nm, dot lattice spacing 3.0 μm) were also prepared in ultra-high vacuum by atomically controlled evaporation through a mask previously prepared with e-beam lithography [96] and positioned on a freshly cleaved MgO(100) single-crystal surface. Also in this case, the arrays of micrometric Fe dots have been capped with a 10 nm thick MgO layer, to avoid oxidation during the subsequent, *ex situ* morphological and magnetic analysis.

The surface morphology and overall shape of the features were studied by *in situ* high-resolution SEM and by *ex situ* atomic force microscopy (AFM) operating in contact mode. The magnetization reversal of mask-deposited Fe micropatterns was studied by MOKE and compared to a continuous Fe film. A continuous Fe film exhibits a well defined uniaxial anisotropy, with an easy axis of magnetization at the reference angle $\theta = 0°$ corresponding to one of the major symmetry axes of the pattern and to the [110] crystal axis of the MgO substrate. On the patterned area the nucleation of the magnetization reversal is anticipated compared with the continuous film, due to the additional magnetostatic energy contribution introduced by the lateral confinement. The magnetic anisotropy of the patterns is changed from uniaxial to biaxial and, thus, it is clearly related to the square lattice symmetry. There are now two easy magnetization directions at $\theta = 90°$ and $0°$, while the hard direction is at $\theta = 45°$. The slight asymmetry between the two easy directions is reminiscent of the original uniaxial anisotropy of the continuous film. The close relationship between the anisotropy directions and the pattern lattice axes provides clear evidence that the new anisotropy originates from the interdot dipolar coupling interaction.

6. The Co/MgO system

Other systems, like Co/MgO(001), were studied to a much lesser extent. Previous papers on nanometre-thick cobalt layers grown on the MgO surface by magnetron sputtering [97, 98]

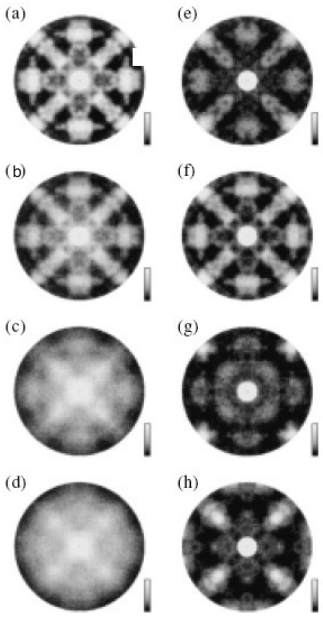

Figure 15. (a)–(d) The patterns of scattering of 1 keV electrons from a MgO(001) crystal with (a) an atomically clean surface and (b)–(d) with cobalt films of various thicknesses: (b) 5 Å; (c) 10 Å; (d) 20 Å. (e)–(h) The results of modelling the experimental patterns in the cluster approximation of single scattering for an MgO(001) single crystal with (e) a clean surface and with (g) an epitaxial fcc cobalt film and (h) an epitaxial hcp cobalt film composed of the grains of two types; (f) a linear superposition of patterns (a), (g), and (h) with the weight coefficients 50, 30, and 20%. Reprinted from [99] with permission.

showed that their magnetic and optical properties significantly depend both on the thickness of cobalt layers and on their structure.

We investigated the growth mechanism and the atomic structure of ultrathin cobalt layers prepared on an MgO(001) single-crystal surface by MBE under ultrahigh-vacuum conditions [99]. The study was performed using AES, LEED, PDMEE [18–20] and SEI [66, 67].

Typical SEI two-dimensional (2D) intensity plots are shown in figures 15(a)–(d) for the MgO(001) cleaved surface and for increasing Co deposition, obtained by a standard LEED apparatus using a primary electron beam of 1 keV in normal incidence. The plots are the stereographic projection (linear black-and-white scale) of the intensity of backscattered electrons with respect to the polar (0°–360°) and azimuthal (7°–46°) escape angles (the brightest regions correspond to the intensity maxima). The main features in the intensity distribution are related to the forward focusing of inelastically backscattered electrons escaping along the most closely packed, crystalline atomic chains [100]. This method therefore probes the real-space crystal structure of the near-surface region [66, 67]. The most anisotropic pattern is observed for an MgO(001) crystal sample with atomically clean surface (figure 15(a)). This 2D plot exhibits a fourfold mirror-rotational symmetry characteristic of the rock-salt crystalline structure along the (001) direction.

We have also modelled the 2D intensity plot from an MgO(001) single-crystal surface within the framework of a single-scattering cluster model [68] (figure 15(e)). A comparison of the patterns in figures 15(a) and (e) shows that all the significant features of the experimental

pattern are well reproduced by the model calculation. Therefore, this approach has also been used for the simulation of patterns of cobalt films deposited onto the substrate surface.

The deposition of cobalt leads to a significant decrease in the intensity anisotropy of 2D plots and to a redistribution of the intensity between various diffraction maxima. Changes in the 2D plots are related to (i) a decrease in the MgO substrate contribution to the observed pattern and (ii) to the gradual formation of a Co film with its own structure(s). The latter effect is expected to become predominant when the deposited metal thickness exceeds ∼10 Å (figures 15(c) and (d)). It should be emphasized, however, that the diffraction patterns retain their fourfold symmetry. This rules out the formation of a hexagonal close packed (hcp) Co structure with an epitaxial hcp(001) ‖ MgO(001) relationship with the substrate. The possibility of a different epitaxial relation, namely, hcp(100) ‖ MgO(001), is suggested by the close values of the c and a lattice parameters for the cobalt and substrate (4.07 and 4.21 Å, respectively), with a difference of only 3.3%. The surface of the film must contain approximately equal numbers of cobalt grains in which the hcp[001] directions are parallel to the MgO[100] and MgO[010] axes. A plot calculated for such a system is shown in figure 15(h), and quite satisfactorily reproduces all the main features of the experimental distribution measured for a 20 Å thick cobalt layer (figure 15(d)). Cobalt can also assume a metastable face-centred cubic (fcc) structure. Therefore, it is necessary to consider the possibility of a cobalt layer growth with the epitaxial relation fcc(001) ‖ MgO(001), which also gives a diffraction pattern with a fourfold symmetry.

In order to elucidate the actual crystal structure of the cobalt films formed in the initial stage of deposition, the measured patterns were analysed assuming each pattern to be a weighted superposition of standard patterns of the substrate and of the possible Co crystal phases [101]. Best fits are evaluated in terms of the R-factors. Using the patterns 15(a), (g) and (h) as the standard components and applying the aforementioned approach, we succeeded in modelling the experimental results with a quite satisfactory accuracy. This is confirmed by a comparison (figures 15(b) and (f)) of the pattern corresponding to 5 Å cobalt deposition with the model pattern obtained assuming ∼50% fractional coverage and 60% fcc + 40% hcp Co crystal structure. This study provides evidence that the Co/MgO(001) system is in fact characterized by an island growth mechanism and by the formation of fcc cobalt grains in the early deposition stages. The statistical weight of the substrate and the two crystalline phases of cobalt varies depending on the deposited layer thickness. The fcc phase dominates below ∼10 Å, while for larger deposition the Co film has predominantly an hcp structure.

7. Conclusions and outlook

We have investigated different metal systems on simple rock-salt oxides, in terms of their structure, morphology and interface chemistry, providing a basis for the understanding of their properties.

Fe on both MgO and NiO(001) surfaces grows in the cubic structure with the (001)Fe ‖ (001)oxide and [110]Fe ‖ [100]oxide orientation.

The Fe/MgO interface is sharp at the atomic level, with a very weak interaction between Fe and MgO up to 400 °C (a temperature higher than the normal operating temperatures of the devices). 'Free standing' Fe films and low-dimensional structures were actually prepared and investigated. Fe submicrometric dots exhibited very peculiar magnetic properties related to the reduced dimensionality.

Co films were also grown on MgO. They present the fcc structure at the early stages of growth and relax to the hcp structure above 10 Å nominal thickness.

At the Fe/NiO(001) interface the oxidation–reduction process involving Fe and NiO results in the formation of an Fe–Ni bct alloyed phase on top of a two-dimensional FeO layer. This

layer is characterized by a 7% expansion of the interplanar distance at the interface with NiO and by a 0.3 Å buckling in the Fe and O atomic positions. The presence of such a structurally distorted FeO phase is predicted to increase the spin magnetic moment of Fe atoms by 0.6 μ_B compared to the ideally abrupt interface.

A reduction of NiO is also induced by the deposition of Au films, which incorporate the metallic Ni atoms, forming an intermixed layer. The reduction takes place at the low-coordination sites at the surface of the NiO film, where kinetic processes remove the more loosely bound oxygen atoms.

In all the investigated systems, given the lower surface free energy of the oxide surfaces compared to the metal ones, the deposited metals tend to form islands, which coalesce above a few monolayers.

Our present and near-future activity in the metal-on-oxide field moves along the following main directions. Top-down techniques such as FIB milling will be continuously improved to achieve smaller nanostructures with improved resolution. New approaches to obtain low-dimensional systems will also be developed. A promising one exploits the self-assembling of metallic particles on spontaneously or artificially patterned substrates. These approaches are expected to give very high densities of ordered structures and narrow nanoparticle size distributions on large areas at a relatively low cost. Vicinal surfaces are a typical example of substrates with periodic steps which can act as nucleation centres for the growth of arrays of one-dimensional periodic structures (see for example [102]). Significant efforts are currently dedicated in our laboratory to the preparation of stepped, 'vicinal' MgO surfaces. Another very promising approach of this kind is represented by the use of regular networks of defects, which can act as nucleation centres for metal cluster formation [103, 104]. The last one seems to be very suitable to pattern oxides in the form of thin films on appropriate substrates and obtain ordered arrays of metal-on-oxide clusters. Finally, the possibility of using refractory metals, such as for example Mo(001), as substrates will allow us to perform heating treatments, which are expected to improve the quality of the patterned oxide films.

Acknowledgments

The authors would like to thank A di Bona, F Boscherini, I I Pronin, F Manghi, V Bellini and A Rota for collaboration in the activities here described. We also acknowledge the financial support by MIUR (PRIN 2003025857, FIRB RBAUO1AW8Y and FIRB RBNE017XSW), MAE (bilateral scientific and technological projects of particular relevance) and the EU (FP6STRP'GSOMEN').

References

[1] Freund H J 2002 *Surf. Sci.* **500** 271
[2] Valden M, Lay X and Goodman D W 1998 *Science* **281** 1647
[3] Haruta M 1997 *Catal. Today* **36** 153
[4] Nogues J and Schuller I K 1999 *J. Magn. Magn. Mater.* **192** 203
[5] De Teresa J M, Barthélémy A, Fert A, Contour J P, Montaigne F and Seneor P 1999 *Science* **286** 507
[6] Luches P, Bellini V, Colonna S, Di Giustino L, Manghi F, Valeri S and Boscherini F 2006 *Phys. Rev. Lett.* **96** 106106
[7] Kuch W, Chelaru L I, Offi F, Wang J, Kotsugi M and Kirschner J 2006 *Nat. Mater.* **5** 128
[8] Moodera J S and Mathon G 1999 *J. Magn. Magn. Mater.* **200** 248
[9] Berkowitz A E and Takano K 1999 *J. Magn. Magn. Mater.* **200** 552
[10] Hufner S 1994 *Adv. Phys.* **43** 183

[11] Fromme B 2001 *d–d Excitations in Transition-Metal Oxides* (*Springer Tracts in Modern Physics* vol 180) (Berlin: Springer)
[12] Luches P, Altieri S, Giovanardi C, Moia T S, Valeri S, Bruno F, Floreano L, Morgante A, Santaniello A, Verdini A, Gotter R and Hibma T 2001 *Thin Solid Films* **400** 139
[13] Giovanardi C, di Bona A, Altieri S, Luches P, Liberati M, Rossi F and Valeri S 2003 *Thin Solid Films* **428** 195
[14] Giovanardi C, di Bona A and Valeri S 2004 *Phys. Rev.* B **69** 075418
[15] Groppo E, Prestipino C, Lamberti C, Luches P, Giovanardi C and Boscherini F 2003 *J. Phys. Chem.* B **107** 4597
[16] Lamberti C, Groppo E, Prestipino C, Casassa S, Ferrari A M, Pisani C, Giovanardi C, Luches P, Valeri S and Boscherini F 2003 *Phys. Rev. Lett.* **91** 46101
[17] Groppo E, Prestipino C, Lamberti C, Carboni R, Boscherini F, Luches P, Valeri S and D'Addato S 2004 *Phys. Rev.* B **70** 165408
[18] Stuck A, Nowicki M, Mroz S, Naumovic D and Ostervalder J 1994 *Surf. Sci.* **306** 21
[19] Valeri S, di Bona A and Gazzadi G C 1994 *Surf. Interface Anal.* **21** 852
[20] Valeri S and di Bona A 1997 *Surf. Rev. Lett.* **4** 141
[21] Valeri S, Altieri S, di Bona A, Luches P, Giovanardi C and Moia T S 2002 *Surf. Sci.* **507–510** 311
[22] Luches P, D'Addato S, Valeri S, Groppo E, Groppo E, Prestipino C, Lamberti C and Boscherini F 2004 *Phys. Rev.* B **69** 045412
[23] Giovanardi C, di Bona A, Moia T S, Valeri S, Pisani C, Sgroi M and Busso M 2002 *Surf. Sci.* **505** L209
[24] Valeri S, Altieri S, del Pennino U, di Bona A, Luches P and Rota A 2002 *Phys. Rev.* B **65** 245410
[25] Benedetti S, Luches P, Liberati M and Valeri S 2004 *Surf. Sci.* **572** L348
[26] Luches P, Liberati M and Valeri S 2003 *Surf. Sci.* **532–535** 409
[27] de Masi R, Reinicke D, Müller F, Steiner P and Hüfner S 2002 *Surf. Sci.* **515** 523
[28] Regan T J, Ohldag H, Stamm C, Nolting F, Lünning J, Stöhr J and White R L 2001 *Phys. Rev.* B **64** 214422
[29] Roosendaal S J, van Asselen B, Elsenaar J W, Vredenberg A M and Habraken F H P M 1999 *Surf. Sci.* **442** 329
[30] Alvarenga A D, Garcia F, Sampaio L C, Giles C, Yokaichiya F, Achete C A, Simaõ R A and Guimarães A P 2001 *J. Magn. Magn. Mater.* **233** 74
[31] Chen Y, Garcia de Abajo F J, Chassé A, Ynzunza R X, Kaduwela A P, Van Hove M A and Fadley C S 1998 *Phys. Rev.* B **58** 13121
[32] Yu G H, Chai C L, Zhu F W, Xiao J M and Lai W Y 2001 *Appl. Phys. Lett.* **78** 1706
[33] Pascarelli S, Boscherini F, D'Acapito F, Hrdy J, Meneghini C and Mobilio S 1996 *J. Synchrotron Radiat.* **3** 147
[34] Newville M *et al* 1995 *Physica* B **154** 208
[35] Zabinsky S I *et al* 1995 *Phys. Rev.* B **52** 2995
[36] Andersen O K 1975 *Phys. Rev.* B **12** 3060
[37] Singh D J 1994 *Planewaves Pseudopotentials and the LPAW Method* (Dordrecht: Kluwer–Academic)
[38] Sjöstedt E, Nordström L and Singh D J 2000 *Solid State Commun.* **114** 15
[39] Madsen G K H *et al* 2001 *Phys. Rev.* B **64** 195134
[40] Blaha P, Schwarz K, Madsen G, Kvasnicka D and Luitz J 1999 *WIEN2k, An Augmented Plane Wave + Local Orbitals Program for Calculating Crystal Properties* Karlheinz Schwarz, Techn. Universität Wien, Austria ISBN 3-9501031-1-2
[41] Perdew J P, Burke S and Ernzerhof M 1996 *Phys. Rev. Lett.* **77** 3865
[42] Chubb S R and Pickett W E 1987 *Phys. Rev. Lett.* **58** 1248
[43] Benedetti S, Torelli P, Luches P, Rota A and Valeri S 2006 *Surf. Sci.* at press
[44] Kumikov V K and Khokonov K B 1983 *J. Appl. Phys.* **54** 1346
[45] Abadias G, Schuster I, Marty A and Gilles B 2000 *Phys. Rev.* B **61** 6495
[46] Nielsen L P, Besenbacher F, Stensgaard I and Laegsgaard E 1993 *Phys. Rev. Lett.* **71** 754
[47] Hubert R A and Gilles J M 1984 *Appl. Surf. Sci.* **22/23** 631
[48] Bertacco R and Ciccacci F 1999 *J. Magn. Magn. Mater.* **196/197** 134
[49] Lairson B M, Visokay M, Sinclair R and Clemens B M 1992 *Appl. Phys. Lett.* **61** 1390
[50] Etienne P, Massies J, Lequien S, Cabanel R and Petroff F 1991 *J. Cryst. Growth* **111** 1003
[51] Park Y, Adenwalla S, Felcher G P and Bader S D 1995 *Phys. Rev.* B **52** 12779
[52] Bate G 1991 *J. Magn. Magn. Mater.* **100** 413
[53] Huang Y Y, Liu C and Felcher G P 1993 *Phys. Rev.* B **47** 183
[54] Thurmer K, Koch R, Weber M and Rieder K H 1995 *Phys. Rev. Lett.* **75** 1767
[55] Chen C C, Yang J, Nakai H and Hashimoto M 2000 *J. Vac. Sci. Technol.* A **18** 819
[56] Fahsold G, Pucci A and Rieder K-H 2000 *Phys. Rev.* B **61** 8475
[57] Lairson B M, Payne A P, Brennan S, Rensing N M, Daniels B J and Clemens B M 1995 *J. Appl. Phys.* **78** 4449
[58] Subagyo A, Sueoka K, Mukasa K and Hayakawa K 1999 *Japan. J. Appl. Phys.* **38** 3820
[59] Fahsold G, Priebe A, Magg N and Pucci A 2000 *Thin Solid Films* **364** 177

[60] di Bona A, Giovanardi C and Valeri S 2002 *Surf. Sci.* **498** 193
[61] Luches P, Benedetti S, Liberati M, Boscherini F, Pronin I I and Valeri S 2005 *Surf. Sci.* **583** 191
[62] Valeri S, Borghi A, Gazzadi G C and di Bona A 1999 *Surf. Sci.* **423** 346
Borghi A, di Bona A, Bisero D and Valeri S 1999 *Appl. Surf. Sci.* **150** 13
[63] Lawler J F, Schad R, Jordan S and van Kempen H 1997 *J. Magn. Magn. Mater.* **165** 224
[64] Urano T and Kanaji T 1988 *J. Phys. Soc. Japan* **57** 3403
[65] Ruby C and Fusy J 1996 *Appl. Surf. Sci.* **99** 393
[66] Pronin I I and Gomoyunova M V 1998 *Prog. Surf. Sci.* **59** 53
[67] Gomoyunova M V and Pronin I I 2001 *Zavod. Lab.* **167** 24
[68] Gomoyunova M V, Pronin I I and Faradzhev N S 1996 *Zh. Eksp. Teor. Fiz.* **110** 311
[69] Suzuki T, Hishita S, Oyoshi K and Souda R 1999 *Surf. Sci.* **442** 291
[70] Lide D R 1990 *CRC Handbook of Chemistry and Physics* (Boston, MA: CRC press)
[71] Meyerheim H L, Popescu R, Kirschner J, Jedrecy N, Sauvage-Simkin M, Heinrich B and Pinchaux R 2001 *Phys. Rev. Lett.* **87** 076102
[72] Meyerheim H L, Popescu R, Jedrecy N, Vedpathak M, Sauvage-Simkin M, Pinchaux R, Heinrich B and Kirschner J 2002 *Phys. Rev.* B **65** 144433
[73] Schieffer P, Krembel C, Hanf M-C and Gewinner G 1999 *J. Electron Spectrosc. Relat. Phenom.* **104** 127
[74] Nannarone S *et al* 2004 *AIP Conf. Proc.* **705** 450
[75] Li C and Freeman A J 1991 *Phys. Rev.* B **43** 780
[76] Osborn J A 1945 *Phys. Rev.* **67** 351
[77] Daughton J M 1999 *J. Magn. Magn. Mater.* **192** 334
[78] Kirk K J, Scheinfein M R, Chapman J N, McVitie S, Gillies M F, Ward B R and Tennant J G 2001 *J. Phys. D: Appl. Phys.* **34** 160
[79] Shi J, Tehrani S, Zhu T, Zheng Y F and Zhu J-G 1999 *Appl. Phys. Lett.* **74** 2525
[80] Johnson J A, Grimsditch M, Metlushko V, Vavassori P, Ilic B, Neuzil P and Kumar R 2000 *Appl. Phys. Lett.* **77** 4410
[81] Cowburn R P, Adeyeye A O and Welland M 1998 *Phys. Rev. Lett.* **81** 5414
[82] Cowburn R P and Welland M 1998 *Appl. Phys. Lett.* **72** 2041
[83] Cowburn R P and Welland M 1998 *Phys. Rev.* B **58** 9217
[84] Vavassori P, Bisero D, Carace F, Liberati M, di Bona A, Gazzadi G C and Valeri S 2005 *J. Magn. Magn. Mater.* **290/291** 183
[85] Valeri S, di Bona A and Vavassori P 2006 Magnetic properties of laterally confined nanometric structures *Trans. Res. Net* Kerala, India.
[86] Melngailis J 1987 *J. Vac. Sci. Technol.* B **5** 469
[87] Gamo K 1997 *Nucl. Instrum. Methods* B **121** 464
[88] Orloff J 1993 *Rev. Sci. Instrum.* **64** 1105
[89] Terris B D, Folks L, Weller D, Baglin J E E, Kellock A J, Rothuizen H and Vettiger P 1999 *Appl. Phys. Lett.* **75** 403
[90] Xiong G, Allwood D A, Cooke M D and Cowburn R P 2001 *Appl. Phys. Lett.* **79** 3461
[91] Russell P E, Stark T J, Griffis D P, Phillips J R and Jarausch K F 1998 *J. Vac. Sci. Technol.* B **16** 2494
[92] Vavassori P 2000 *Appl. Phys. Lett.* **77** 1605
[93] Cowburn R P, Ferré J, Bland J A C and Miltat J 1995 *J. Appl. Phys.* **78** 7210
[94] Donaue M J and Porter D G 2002 *OOMMF User's Guide, Version 1.2 alpha 3* (Gaithersburg, MD: National Institute of Standards and Technology)
[95] Hanson M, Johansson G, Nilsson B, Isberg P and Wäppling R 1999 *J. Appl. Phys.* **85** 2793
[96] Gerardino A *et al* 2001 *Microelectron. Eng.* **57** 931
[97] Sato H and Miyazaki T 1998 *J. Magn. Magn. Mater.* **177–181** 1197
[98] Cai J-W, Okamoto S, Kitakami O and Shimada Y 2001 *Phys. Rev.* B **63** 104418
[99] Pronin I I, Valdaitsev D A, Voronchikhin A S, Gomoyunova M V, Contri S F, Benedetti S, Luches P and Valeri S 2005 *Tech. Phys. Lett.* **31** 494
[100] Gomoyunova M V, Pronin I I and Faradzhev N S 1996 *Zh. Eksp. Teor. Fiz.* **110** 311
[101] Pronin I I, Valdaitsev D A, Faradzhev N S, Gomoyunova M V, Luches P and Valeri S 2001 *Appl. Surf. Sci.* **175/176** 83
[102] Gambardella P, Blanc M, Brune H, Kuhnke K and Kern K 2000 *Phys. Rev.* B **61** 2254
[103] Leroy F, Renaud G, Letoublon A, Lazzari R, Mottet C and Goniakowski J 2005 *Phys. Rev. Lett.* **95** 185501
[104] Shiryaev S Yu, Jensen F, Lundsgaard Hansen J, Wulff Petersen J and Nylandsted Larsen A 1997 *Phys. Rev. Lett.* **78** 503
[105] Kokalj A 2003 *Comput. Mater. Sci.* **28** 155 (code available from http://www.xcrysden.org)